Single-layer, cascaded and broadband-heat-dissipation metasurface for multi-wavelength lasers and infrared camouflage

Xingdong Feng[1,2], Tianqi Zhang[1,2], Xuejun Liu[3], Fan Zhang[3], Jianjun Wang[2,4], Hong Bao[1,2], Shan Jiang[1,2,3,4]* and Yongan Huang[3]*

[1]Hangzhou Institute of Technology, Xidian University, Hangzhou 311200, China; [2]School of Mechano-Electronic Engineering, Xidian University, Xi'an 710071, China; [3]State Key Laboratory of Intelligent Manufacturing Equipment and Technology, Huazhong University of Science and Technology, Wuhan 430074, China; [4]State Key Laboratory of Electromechanical Integrated Manufacturing of High-performance Electronic Equipments, Xidian University, Xi'an 710071, China.

*Correspondence: S Jiang, E-mail: jiangshan@xidian.edu.cn; YA Huang, E-mail: yahuang@hust.edu.cn

This file includes:

Supplementary information for this paper is available at https://doi.org/10.29026/oea.2025.240280
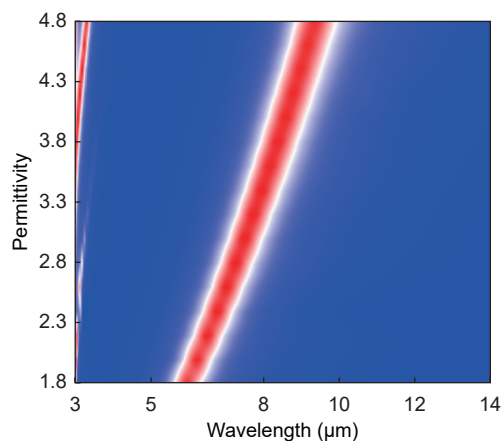
Fig. S1 | Dependence of the absorptance spectra in 3–14 µm on different permittivity.
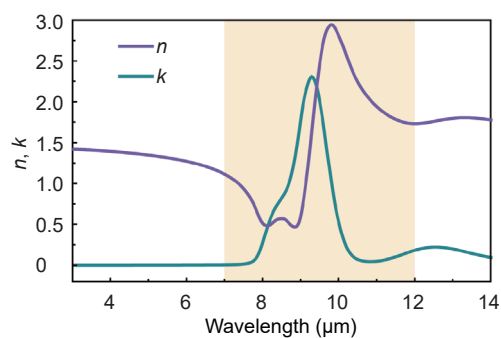

Fig. S2 | The refractive index *n* and extinction efficiency *k* of SiO_2 in 3–14 µm.
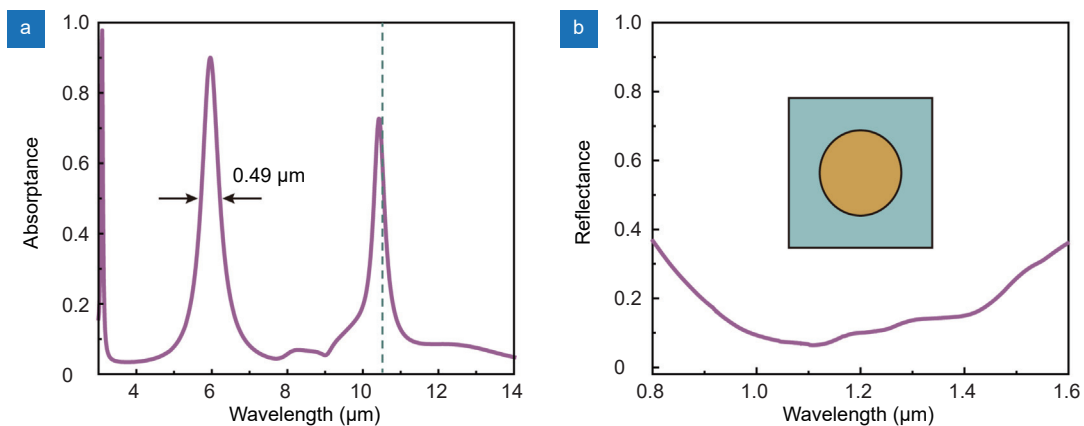
Fig. S3 | Amplitude and phase modulation characteristics of the metasurface with single-sized metallic disks. (**a**) Absorption spectrum in 3–14 µm band, and (**b**) reflection spectrum in 0.8–1.6 µm band.

Fig. S4 | The 3D far-field scattering pattern of the metasurface with single-sized metallic disks at 1.06 μm, showing that the electromagnetic waves are scattered into four non-specular directions.
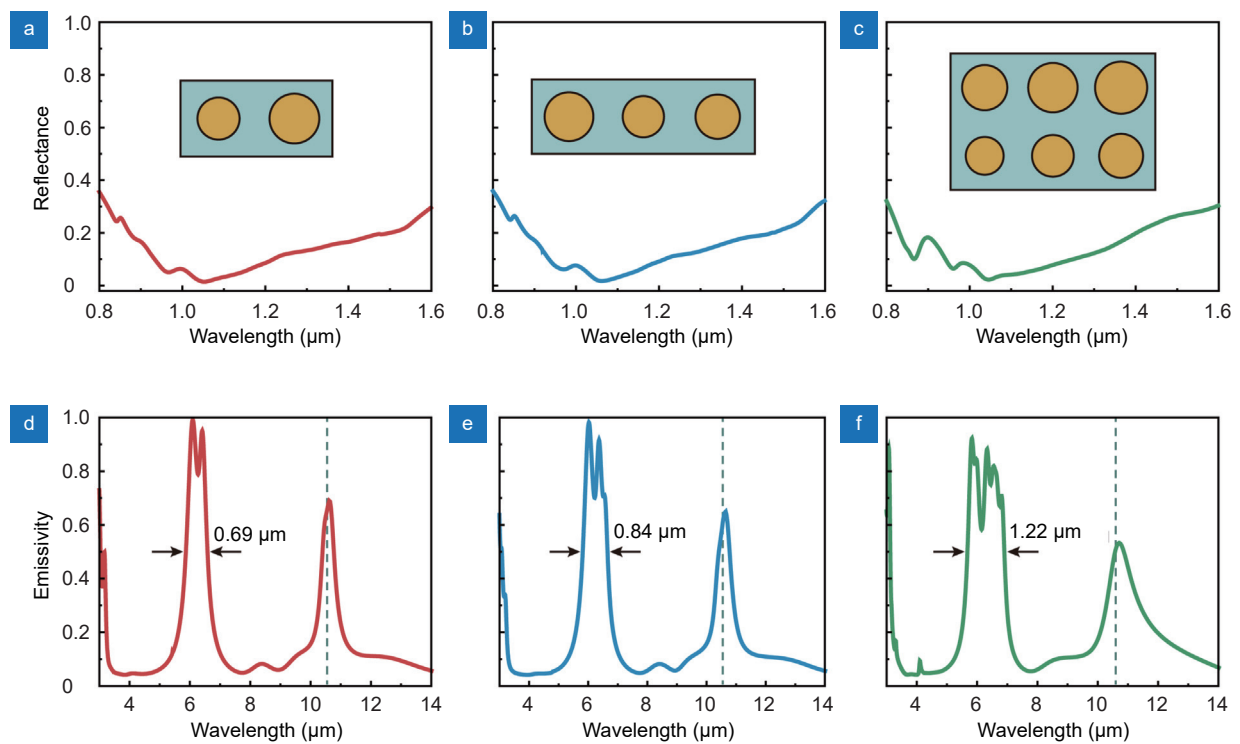
Fig. S5 | Amplitude and phase modulation characteristics of the cascaded metasurfaces with different numbers of resonators.

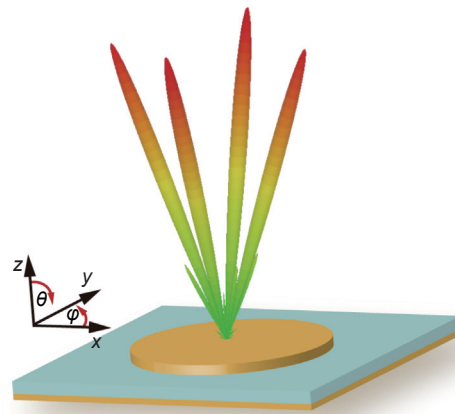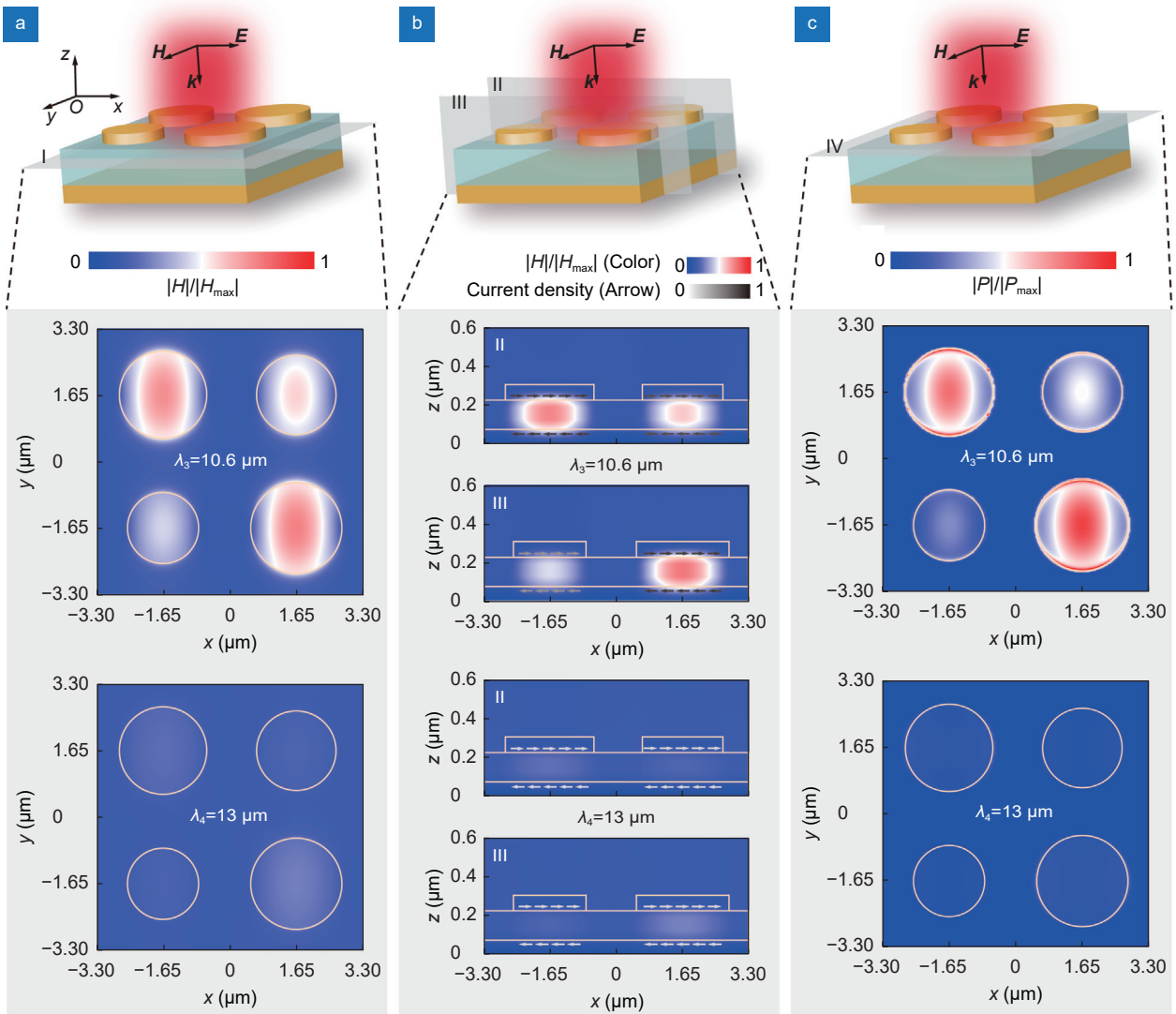**Fig. S6 |** Electromagnetic field distributions of the cascaded metasurface. (**a**) Magnetic field intensity on the *z* = 0.2 μm plane (cross-section I) at 10.6 μm and the non-resonant wavelength of 13 μm. (**b**) Magnetic field intensity and current density on the *y* = ±1.65 μm planes (cross-sections II and III) at 10.6 μm and the non-resonant wavelength of 13 μm. (**c**) Power loss intensity on the *z* = 0.23 μm plane (cross-section IV) at 10.6 μm and the non-resonant wavelength of 13 μm.
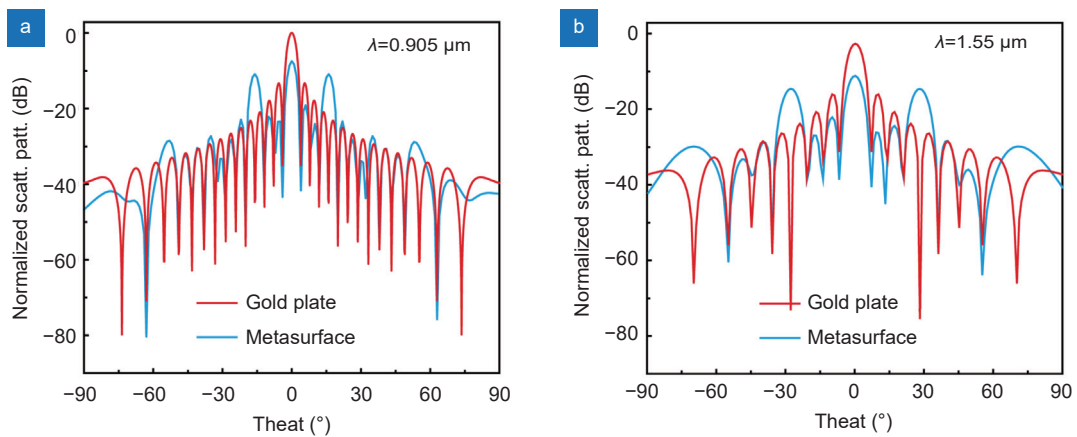
Fig. S7 | The normalized scattering patterns of the metasurface and a gold plate on φ = 90° plane at: (**a**) 0.905 μm and (**b**) 1.55 μm.
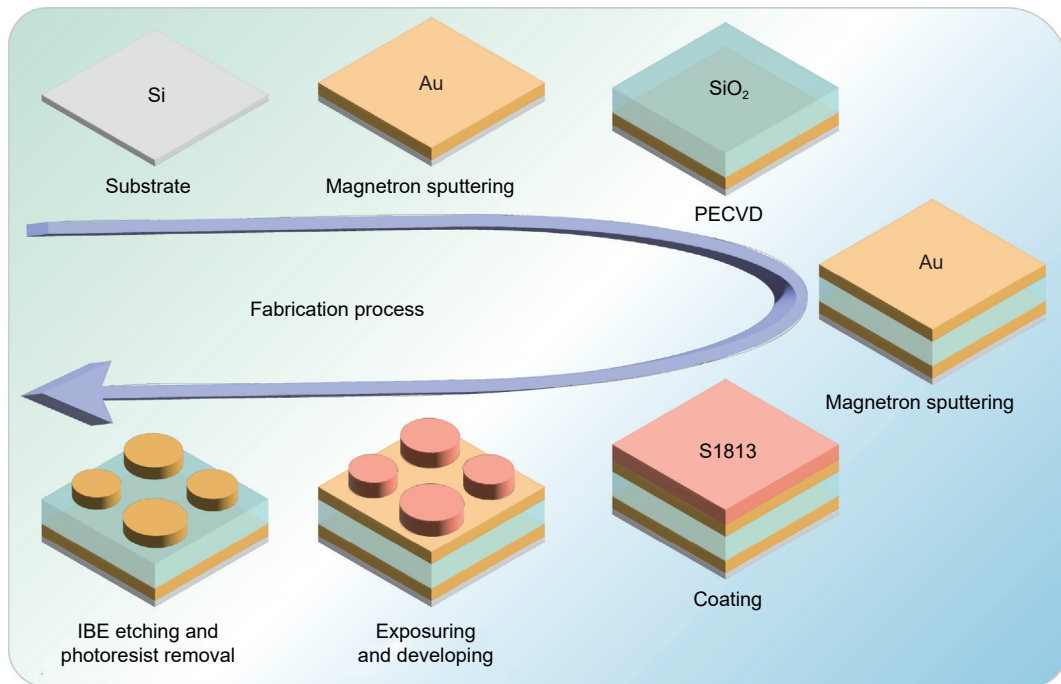
Fig. S8 | Schematic diagram for the fabrication process used for the cascaded metasurface.
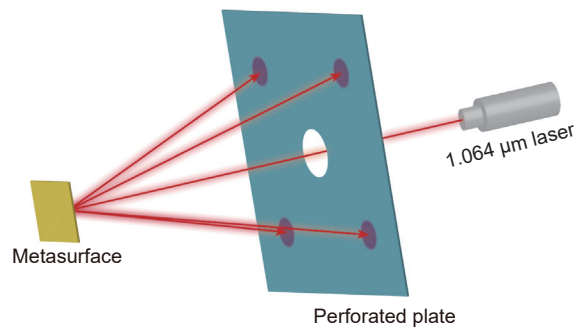
Fig. S9 | The schematic diagram of the experimental setup used to check the laser scattering patterns.
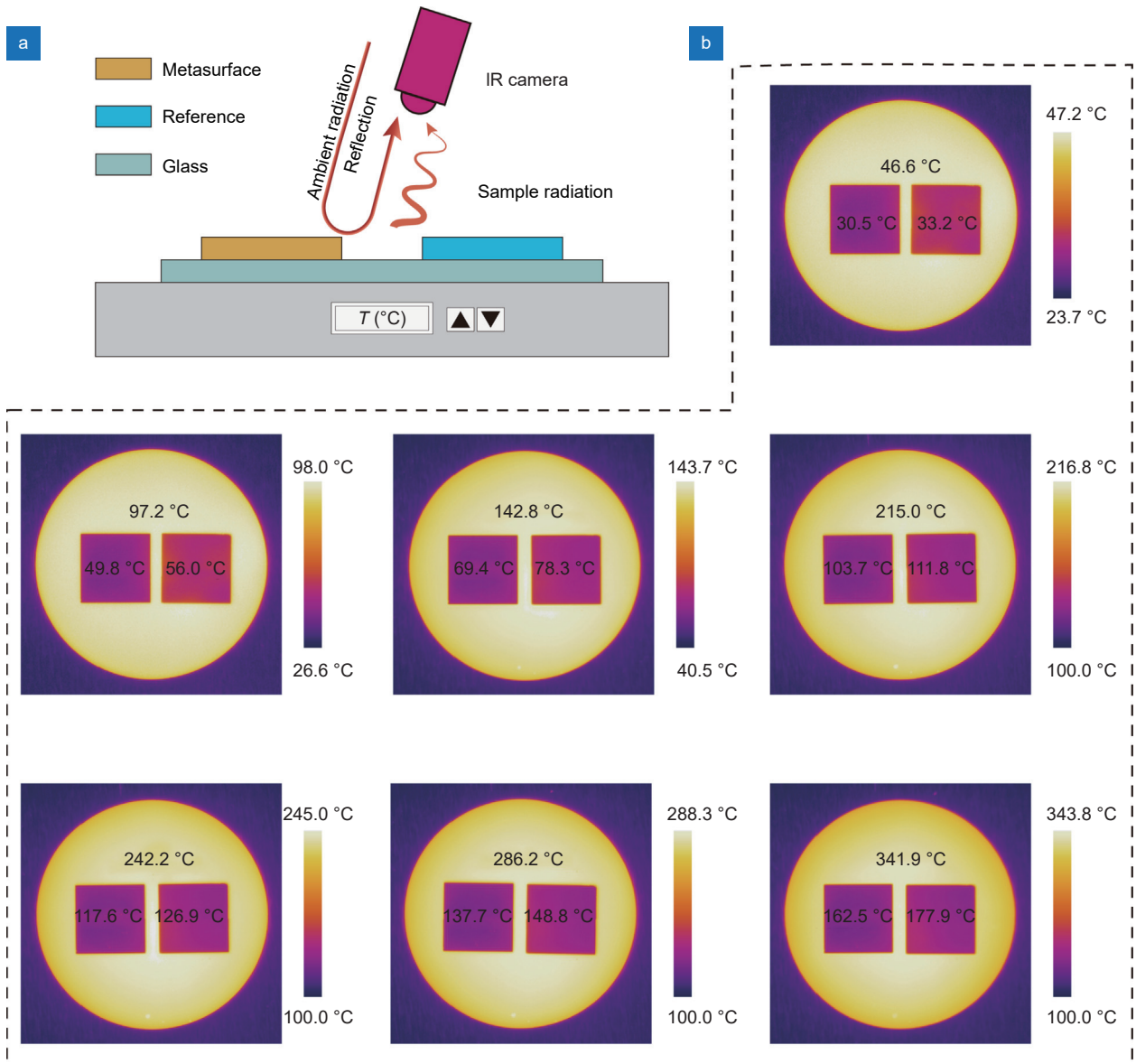
Fig. S10 | Infrared camouflage performance of the metasurface. (**a**) Schematic of the experiment setup for infrared imaging under the same heating temperature. (**b**) The thermal infrared images of the metasurface and reference under different heating temperatures.
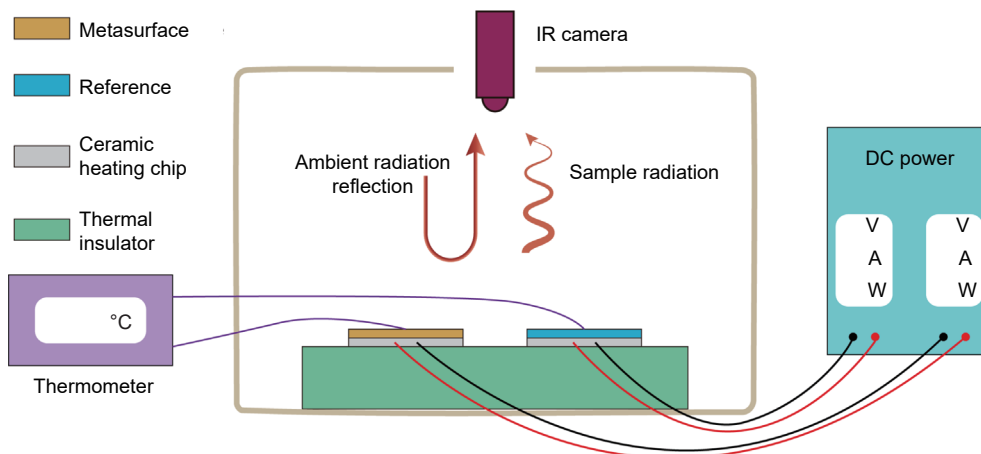
Fig. S11 | The schematic diagram of the heating system for demonstration of the broadband radiative heat dissipation capability.

Section 1: The angular characteristics of multispectral camouflage

To verify the multispectral camouflage performance of the metasurface under different incident angles, we have measured the reflectance spectra in 0.8–1.6 μm and emissivity spectra in 3–14 μm at incident angles of 15°, 30°, and 45°, which are given in Fig. S12. From Fig. S12(a), although the reflectance spectra exhibit a blue shift with increasing incident angle, the metasurface still remains a reflectance below 0.4 across the entire band even at the angle of 45°. Moreover, it keeps the reflectance below 0.2 at the wavelengths of 0.905 μm and 1.06 μm. On the other hand, the resonance peak positions of the metasurface's emissivity spectra hardly change with the variation of incident angle (Fig. S12(b)). The amplitude of emissivity decreases with the rise in incident angle. Although this weakens the thermal dissipation ability of the metasurface in the undetected band, it also reduces its infrared signals within the detected bands (especially in the LWIR band). Based on the above analysis, the metasurface exhibits good wide-angle response characteristics, which is significant for its practical applications.
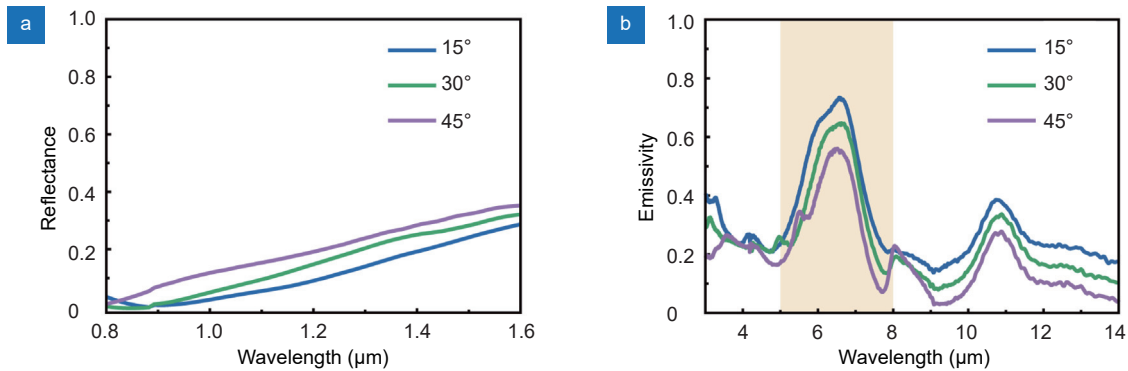
Fig. S12 | The angular characteristics of multispectral camouflage. (**a**) The reflectance spectra in 0.8–1.6 μm and (**b**) emissivity spectra in 3–14 μm at incident angles of 15°, 30°, and 45°.

Section 2: The spectral irradiance and total camouflage performance (TCP) of the metasurface

To quantify the IR signal reduction and energy dissipation of the metasurface, we first calculated its spectral irradiance. Based on the Planck's law, the spectral blackbody emissive power can be calculated by the following equation[S1]

$$E_{\rm b}(\lambda, T) = \frac{2\pi h c^2}{\lambda^5 \exp\left(\dfrac{hc}{\lambda k_{\rm B} T} - 1\right)} \ , \tag{S1}$$

where λ, T, h, c, $k_{\rm B}$, are the wavelength, temperature, Planck's constant, speed of light, and Boltzmann constant, respectively. The spectral irradiance of the metasurface compared to a blackbody and gold film is presented in Fig. S13 (T =
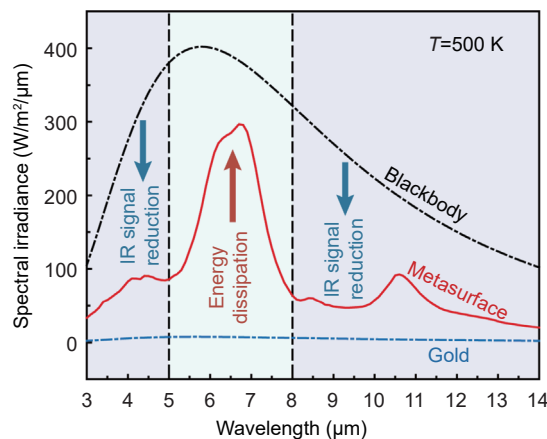
Fig. S13 | The spectral irradiance of the metasurface compared to a blackbody and gold film (T=500 K).

500 K). The blackbody represents an ideal energy dissipation object with an emissivity of 1, while the gold film has nearly perfect infrared signature reduction but lacks thermal management capability.

In the following, the emissive power in various bands (3–5 μm, 5–8 μm, and 8–14 μm) can be obtained by discretizing the equation as a function of wavelength as follows:

$$E_{\lambda_1-\lambda_2}(T) = \int_{\lambda_1}^{\lambda_2} \varepsilon(\lambda,\ T) M_{\mathrm{b}}(\lambda,\ T) \cong \sum \varepsilon(\lambda,\ T) E_{\mathrm{b}}(\lambda,\ T)\Delta\lambda\ , \tag{S2}$$

where λ_1, λ_2, and $\varepsilon(\lambda,\ T)$ are the shortest wavelength of the band, the longest wavelength of the band, and spectral emissivity, respectively. To investigate the IR signal reduction capability of the metasurface, we compared the radiated energy of the metasurface and a blackbody within the two detected bands (3–5 μm and 8–14 μm). Taking a temperature of 500 K as an example, the emissive power by the metasurface in the 3–5 μm and 8–14 μm bands is 149.96 W/m² and 293.01 W/m², respectively, which are 27.2% and 25.9% of the blackbody. This demonstrates that the metasurface has excellent capability to suppress IR signals within these two detected bands. At the same time, the emissive power of the metasurface in the non-atmospheric window is 2506% higher than that of the gold film, indicating its capacity for high-performance energy dissipation.

In addition, based on Eq. (S2), we calculate the emissive energy for each band at different temperatures, with the results shown in Fig. S14(a). The emissive energy distribution of a blackbody follows Wien's Displacement Law, which states that the peak of the spectral blackbody emissive power shifts toward shorter wavelengths as the temperature increases. At lower temperatures, the peak of the spectral blackbody emissive power lies within the 8–14 μm band. As seen from Fig. S14(a), when the temperature is below 350 K, the metasurface emits more energy in the 8–14 μm band than in the 5–8 μm band. At this point, the thermal dissipation effect resulting from the high emissivity of the metasurface in the 5–8 μm band is relatively minor. As the temperature rises, the energy dissipation from the undetected window gradually becomes dominant.
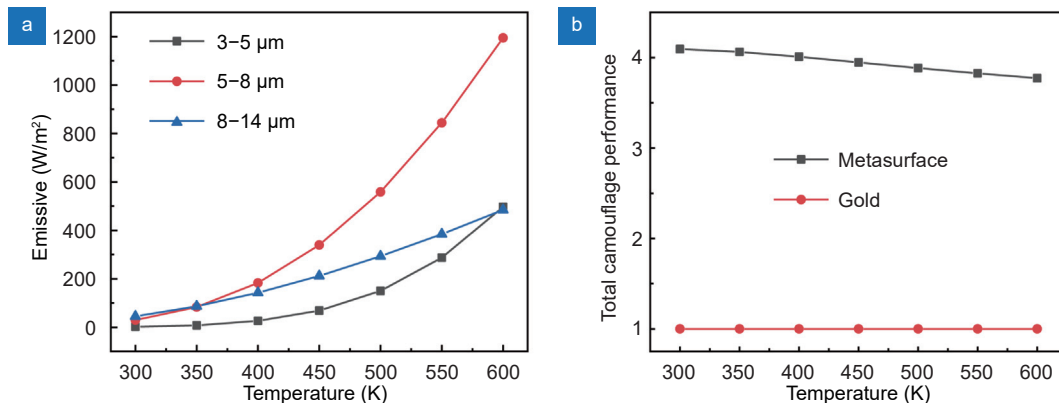
Fig. S14 | (**a**) Emissive power in different bands and (**b**) the total camouflage performance (TCP) of the metasurface at different temperatures.

Based on the above analysis, it is evident that the emissive power of the metasurface in both the detected bands and the undetected band will influence its infrared camouflage performance. To more comprehensively evaluate the infrared camouflage performance of the materials, the total camouflage performance (TCP) was introduced[S1], which integrates the effect of IR signal reduction, thermal dissipation, and temperature on the infrared camouflage performance. In ref.[S1], TCP is defined as:

$$\mathrm{TCP} = \mathrm{CP}(\lambda_1 - \lambda_2) \cdot \mathrm{CP}(\lambda_3 - \lambda_4)\ , \tag{S3}$$

where camouflage performance of single band (CP) corresponds to the dissipation energy ratio over the reduction energy ratio of each band, which is determined as follows

$$\mathrm{CP} = \phi_{\mathrm{undetected\ band}}/\phi_{\mathrm{detected\ band}}\ , \tag{S4}$$

where ϕ is the emissive power ratio at each band from λ_1 to λ_2 between the designed (i.e., metasurface) and reference surface (i.e., gold), and can be determined as follows

$$\phi_{\lambda_1-\lambda_2} = E_{\lambda_1-\lambda_2,\,\text{designed surface}} \big/ E_{\lambda_1-\lambda_2,\,\text{reference surface}} \, . \tag{S5}$$

The TCP values at different temperatures are calculated based on Eqs. (5, 6), as depicted in Fig. S14(b). The fabricated metasurface in this work can maintain a TCP close to 4 across various temperatures, which is lower than that reported in ref.[S1] due to the higher infrared emissivity of our metasurface in the two detected bands. It is worth noting that in the undetected band, the emissive power of our metasurface is higher than that of the metasurface reported in ref.[S1]. In summary, our metasurface can reduce the IR signal in two detected bands while maintaining efficient heat dissipation in the non-atmospheric window, thereby achieving excellent infrared camouflage performance and thermal stability.

Table S1 | Comparison between our work and the existing works.

Ref.	Number of layers (Thickness)	IR camouflge	Thermal management	Laser camouflage
Design platform: 1D-PCs				
ref.[S2]	3 (0.45 μm)	$\varepsilon_{3-5\,\mu m} = 0.25$; $\varepsilon_{8-14\,\mu m} = 0.33$	Yes, $\varepsilon_{5-8\,\mu m} = 0.77$	10.6 μm
ref.[S3]	4 (2.461 μm)	$\varepsilon_{8-14\,\mu m} < 0.2$	No	No
ref.[S4]	8 (4.308 μm)	$\varepsilon_{3-5\,\mu m} = 0.21$; $\varepsilon_{8-14\,\mu m} = 0.16$	Yes, $\varepsilon_{5-8\,\mu m} = 0.54$	1.06 μm, 1.55 μm, and 10.6 μm
ref.[S5]	11 (6.732 μm)	$\varepsilon_{3-5\,\mu m} = 0.11$; $\varepsilon_{8-14\,\mu m} = 0.12$	Yes, $\varepsilon_{5-8\,\mu m} = 0.61$	1.55 μm and 10.6 μm
Design platform: Metamaterial				
Ref.	Number of layers (Thickness)	IR camouflge	Thermal management	Laser camouflage
ref.[S1]	3 (0.6 μm)	Low emissivity	Yes, Narrowband emission	No
ref.[S6]	3 (0.62 μm)	$\varepsilon_{3-5\,\mu m} = 0.21$; $\varepsilon_{8-14\,\mu m} = 0.19$	Yes, $\varepsilon_{5-8\,\mu m} = 0.43$	10.6 μm
ref.[S7]	4 (0.357 μm)	Low emissivity	No	1.06 μm and 10.6 μm
ref.[S8]	5 (0.4 μm)	$\varepsilon_{3-5\,\mu m} = 0.24$; $\varepsilon_{8-14\,\mu m} = 0.11$	Yes, $\varepsilon_{5-8\,\mu m} = 0.57$	No
ref.[S9]	5 (0.55 μm)	$\varepsilon_{3-5\,\mu m} = 0.35$; $\varepsilon_{8-14\,\mu m} = 0.46$	Yes, $\varepsilon_{5-8\,\mu m} = 0.66$	0.8–1.6 μm and 10.6 μm
ref.[S10]	5 (0.7 μm)	$\varepsilon_{8-14\,\mu m} < 0.2$	Yes, $\varepsilon_{5-8\,\mu m} = 0.6$	No
ref.[S11]	One step (2.7 μm)	Low emissivity	No	8–14 μm
ref.[S12]	Two step (3.07 μm)	$\varepsilon_{3-5\,\mu m} < 0.25$; $\varepsilon_{8-14\,\mu m} < 0.33$	No	0.9–1.2 μm and 9–12 μm
ref.[S13]	One step and 4 layer (2.719 μm)	$\varepsilon_{3-5\,\mu m} = 0.19$; $\varepsilon_{8-14\,\mu m} = 0.33$	No	1.06 μm, 1.55μm, and 8–14 μm
Our work	3 (0.3 μm)	$\varepsilon_{3-5\,\mu m} = 0.31$; $\varepsilon_{8-14\,\mu m} = 0.275$	Yes, $\varepsilon_{5-8\,\mu m} = 0.51$	0.8–1.6 μm and 10.6 μm

References

S1.   Lee N, Kim T, Lim JS et al. Metamaterial-selective emitter for maximizing infrared camouflage performance with energy dissipation. *ACS Appl Mater Interfaces* **11**, 21250–21257 (2019).

S2.   Pan MY, Huang Y, Li Q et al. Multi-band middle-infrared-compatible camouflage with thermal management via simple photonic structures. *Nano Energy* **69**, 104449 (2020).

S3.   Xi W, Lee YJ, Yu SL et al. Ultrahigh-efficient material informatics inverse design of thermal metamaterials for visible-infrared-compatible camouflage. *Nat Commun* **14**, 4694 (2023).

S4.   Jiang XP, Yuan H, He X et al. Implementing of infrared camouflage with thermal management based on inverse design and hierarchical metamaterial. *Nanophotonics* **12**, 1891–1902 (2023).

S5.   Zhu HZ, Li Q, Tao CN et al. Multispectral camouflage for infrared, visible, lasers and microwave with radiative cooling. *Nat Commun* **12**, 1805 (2021).

S6.   Yu K, Zhang W, Qian MD et al. Multiband metamaterial emitters for infrared and laser compatible stealth with thermal management based on dissipative dielectrics. *Photonics Res* **11**, 290–298 (2023).

S7.   Zhang CL, Huang C, Pu MB et al. Dual-band wide-angle metamaterial perfect absorber based on the combination of localized surface

plasmon resonance and Helmholtz resonance. *Sci Rep* **7**, 5652 (2017).

S8. Wu YJ, Luo J, Pu MB et al. Optically transparent infrared selective emitter for visible-infrared compatible camouflage. *Opt Express* **30**, 17259–17269 (2022).

S9. Liu XH, Wang P, Xiao CY et al. A bioinspired bilevel metamaterial for multispectral manipulation toward visible, multi‐wavelength detection lasers and mid‐infrared selective radiation. *Adv Mater* **35**, 2302844 (2023).

S10. Lim JS, Lee N, Kim T et al. Multiresonant selective emitter with enhanced thermal management for infrared camouflage. *ACS Appl Mater Interfaces* **16**, 15416–15425 (2024).

S11. Xie X, Li X, Pu MB et al. Plasmonic metasurfaces for simultaneous thermal infrared invisibility and holographic illusion. *Adv Funct Mater* **28**, 1706673 (2018).

S12. Feng XD, Pu MB, Zhang F et al. Large-area low-cost multiscale-hierarchical metasurfaces for multispectral compatible camouflage of dual-band lasers, infrared and microwave. *Adv Funct Mater* **32**, 2205547 (2022).

S13. Huang JK, Wang YT, Yuan LM et al. Large‐area and flexible plasmonic metasurface for laser–infrared compatible camouflage. *Laser Photonics Rev* **17**, 2200616 (2023).